



Broadband Variability and Correlation Study of 3C 279 during Flares of 2017–2018

Raj Prince

Raman Research Institute, Sadashivanagar, Bangalore 560080, India; rajprince@rri.res.in

Received 2019 July 12; revised 2020 January 1; accepted 2020 January 12; published 2020 February 25

Abstract

A multiwavelength temporal and spectral analysis of flares of 3C 279 during 2017 November–2018 July are presented in this work. Three bright gamma-ray flares were observed simultaneously in X-ray and optical/UV along with a prolonged quiescent state. A “harder-when-brighter” trend is observed in both gamma-rays and X-rays during the flaring period. The gamma-ray light curve for all the flares is binned in one day time bins and a day-scale variability is observed. Variability time constrains the size and location of the emission region to 2.1×10^{16} cm and 4.4×10^{17} cm, respectively. The fractional variability reveals that the source is more than 100% variable in gamma-rays and it decreases toward the lower energy. A cross-correlation study of the emission from different wavebands is done using the discrete correlations function method, which shows a strong correlation between them without any time lags. The zero time lag between different wavebands suggests their cospatial origin. This is the first time 3C 279 has shown a strong correlation between gamma-ray and X-ray emission with zero time lag. A single-zone emission model was adopted to model the multiwavelength spectral energy distributions by using the publicly available code GAMERA. The study reveals that a higher jet power in electrons is required to explain the gamma-ray flux during the flaring state, as much as 10 times that required for the quiescent state. However, more jet power in the magnetic field has been observed during the quiescent state compared to the flaring state.

Unified Astronomy Thesaurus concepts: [Active galaxies \(17\)](#); [Quasars \(1319\)](#); [Jets \(870\)](#); [Gamma-rays \(637\)](#); [Blazars \(164\)](#); [Galactic and extragalactic astronomy \(563\)](#)

1. Introduction

Blazars are a class of active galactic nuclei whose jets are oriented close to the observer’s line of sight (Urry & Padovani 1995). In general, blazars exhibit highly luminous and rapidly variable nonthermal continuum emission across the entire electromagnetic (EM) spectrum extending from radio to very high energy gamma-ray. A wide range of variability time across the whole electromagnetic spectrum is found in most of the blazars. A timescale of variability ranging from minutes to years is inferred for blazars (Aharonian et al. 2007; Raiteri & Villata 2013). Blazars are generally classified into two categories viz., BL Lac objects and flat spectrum radio quasar FSRQ, depending upon their optical spectra. BL Lac objects show a very weak or no emission line in their optical spectra, while on the other hand FSRQs are known for their strong, broad emission lines. The highly energetic phenomena inside the blazars are detected as strong and spectacular flares across the EM spectrum, with rapid variability. There have been several studies on the blazar to understand the broadband flaring activity, but the origin of fast variability is not well understood. The observed broadband spectral energy distribution (SED) of a blazar shows two peaks, one extending from radio to optical, and another ranging from X-ray to gamma-ray. The low energy radiation from radio to UV/X-ray is caused by synchrotron radiation of relativistic electrons accelerated inside the jet. In leptonic models, the high energy gamma-ray radiation is caused by inverse Compton (IC) scattering of soft target photons originating in synchrotron radiation (SSC; Sikora et al. 2009) or external photon fields (EC; Dermer et al. 1992; Sikora et al. 1994).

3C 279 has been classified as an FSRQ at redshift, z of 0.536 (Lynds et al. 1965), and is a well-studied blazar in its class. The mass of the black hole was estimated in the range of

$(3-8) \times 10^8 M_{\odot}$ by Woo & Urry (2002), Gu et al. (2001), and Nilsson et al. (2009) from the luminosity of broad optical emission lines, the width of the H_{β} lines, and from the luminosity of the host galaxy, respectively. Fermi-LAT has been continuously monitoring 3C 279 since 2008, and along with that it is also monitored by different other facilities in X-ray, optical, and radio. The blazar 3C 279 has been widely studied in the past throughout the EM spectrum. The previous multiwavelength studies showed that the gamma-ray emission region in 3C 279 lies close to the base of the jet, at subparsec scale (Hayashida et al. 2015; Paliya 2015; Paliya et al. 2016). However, the recent study by Patino-Alvarez et al. (2019) found evidence of high energy emission emitted at much greater distance from the core, at ~ 42 pc. Further, multi-wavelength study on this source will help the community to probe the location of the gamma-ray emission region along the jet axis.

The correlation study between optical polarization (degree/angle) and gamma-rays give strong evidence for the synchrotron and Compton model, and suggest that the jet structure is not axisymmetric (Abdo et al. 2010). The above correlation also suggests the presence of a helical magnetic field component (Zhang et al. 2015). The rate of change of the polarization angle (PA) with fast variability time suggests a compact emission region, close to the central black hole, located at a distance along the jet. A detailed correlations study between optical and gamma-ray has been done for a sample of blazars by Cohen et al. (2014), and they have found a time lag of 110 days between optical and gamma-ray emission. A similar study has been done by Hayashida et al. (2012) for 3C 279 and they have noticed a lag of 10 days between optical and gamma-ray emission. They also found that the X-ray and gamma-ray emissions are not well correlated, and the nature of X-ray emission in a blazar is still unclear. A correlation study

between radio and gamma-rays was also performed by Pushkarev et al. (2010), and they noticed that in a sample of 183 blazars most of them show that the radio flares lag the gamma-ray flare. A similar result was found in the case of Ton 599 by Prince (2019), where a lag of 27 days was noticed between radio and gamma-rays. Keeping consistency with results from earlier studies, here I try to investigate the possible correlation between different wavelengths during the 2017–2018 flare of 3C 279.

2. Multiwavelength Observations and Data Analysis

2.1. Fermi-LAT

Fermi-LAT is a pair conversion γ -ray telescope sensitive to photon energies between 20 MeV to higher than 500 GeV, with a field of view (FOV) of about 2.4 sr (Atwood et al. 2009). The LAT’s FOV covers about 20% of the sky at any time, and it scans the whole sky every three hours. NASA launched the instrument in 2008 into a near-Earth orbit. *Fermi*-LAT has been continuously monitoring 3C 279 since 2008 August. The standard data reduction and analysis procedure¹ has been followed. I have chosen a circular region of radius 10° around the source of interest during the analysis. This circular region is also known as the region of interest. Further analysis procedure is the same as given in Prince et al. (2018). I have analyzed the *Fermi*-LAT data for 3C 279 from 2017 November to 2018 July and found that the source has shown three significant flares in these nine months.

2.2. Swift-XRT/UVOT

Swift-XRT/UVOT is the space-based telescope which observes the galactic as well as extragalactic sources in X-rays, opticals, and UV simultaneously. Fermi detected blazars could also be observed by the *Swift*-XRT/UVOT telescope as a monitoring program as well as a time-of-opportunity program. The blazar 3C 279 was observed by *Swift*-XRT/UVOT when it was flaring during 2017–2018, and the details of the observations are present in Table 1. I processed the XRT data by using the task “xrtpipeline” version 0.13.2, which produces the cleaned event files for each observation. While reprocessing the raw data, I have used the latest calibration files (CALDB version 20160609). The cleaned event files are produced only to the Photon Counting mode observations. The task “xrtpipeline” is used to select the source and the background region. Circular regions of radius $20''$ around the source and slightly away from the source (fewer photon counts) are chosen for the source and the background regions, respectively. The X-ray spectra were extracted in “xselect” and used as input spectra in “Xspec” for modeling. A simple power-law (PL) model with the galactic absorption column density $n_H = 1.77 \times 10^{20} \text{ cm}^{-2}$ (Kalberla et al. 2005) is used to model the XRT spectra.

Simultaneous to XRT, the *Swift* Ultraviolet/Optical Telescope (UVOT; Roming et al. 2005) has also observed 3C 279 in all the available six filters *U*, *V*, *B*, *W1*, *M2*, and *W2*. The image is extracted by selecting a circular region of $5''$ around the source and a circular region of $10''$ away from the source for the background. The task “uvotimsum” is used to sum the multiple observations in the same filter at the same epoch, and further, the task “uvotsource” is used to extract the source

Table 1

Log of the Observations from *Swift*-XRT/UVOT Telescope During the Flaring State (MJD 58050–58350)

Obs-ID	Exposure (ks)
00035019201	1.9
00035019203	1.8
00035019204	2.0
00035019206	0.5
00035019210	0.9
00035019211	0.9
00035019213	0.6
00035019214	0.9
00035019218	1.1
00035019219	1.0
00035019220	1.2
00035019221	2.1
00035019222	1.7
00035019224	1.8
00035019225	1.6
00035019227	2.5
00035019228	0.2
00035019229	0.7
00035019230	2.0
00035019231	2.0
00035019232	2.0
00035019233	2.1
00035019234	1.5
00035019235	0.8
00035019236	1.6
00035019237	0.5
00035019238	1.5
00035019239	1.5
00035019240	1.5
00035019241	1.1
00035019242	1.1
00030867052	1.0
00030867054	1.4
00030867055	0.4
00030867056	1.1
00030867057	1.0
00030867058	1.0
00030867059	1.0
00030867060	1.1
00030867061	0.5
00030867062	1.2
00030867063	0.6
00030867064	1.1

magnitudes and fluxes. Magnitudes are corrected for galactic extinction using $R_V = A_V/E(B-V) = 3.1$ and $E(B-V) = 0.025$ (Schlafly & Finkbeiner 2011) and converted into flux using the zero-points (Breeveld et al. 2011) and conversion factors (Larionov et al. 2016).

2.3. Steward Optical Observatory

Steward Optical Observatory is a part of the *Fermi* multiwavelength support program. It provides the optical data for the LAT-monitored blazars and also measures the linear optical polarization. Archival data from the Steward Optical Observatory, Arizona (Smith et al. 2009)² has been used in this particular study.

¹ <https://fermi.gsfc.nasa.gov/ssc/data/analysis/documentation/>

² <http://james.as.arizona.edu/~psmith/Fermi/DATA/individual.html>

3C 279 is being continuously monitored with the SPOL CCD Imaging/Spectrometer of the Steward Observatory. Optical *V*-band and *R*-band photometric and polarimetric (degree of polarization (DoP) and position angle) data is collected for the flaring period of 3C 279 from 2017 November to 2018 July.

2.4. Radio Data at 15 and 230 GHz

Owens Valley Radio Observatory (OVRO; Richards et al. (2011) is also a part of the *Fermi* monitoring program. It monitors the Fermi blazars by a 40 m single disk antenna at a frequency of 15 GHz. More than 1800 Fermi blazars are being continuously monitored by OVRO twice a week. 3C 279 is one of them, and I have collected the radio data at 15 GHz from 2017 November to 2018 July.

The Submillimeter Array provided the 230 GHz data (SMA) from the observer center database (Gurwell et al. 2007). The data is collected for the period of nine months from 2017 November to 2018 July.

3. Results and Discussions

I have analyzed the *Fermi*-LAT and *Swift*-XRT/UVOT data from 2017 November to 2018 July (MJD 58060–MJD 58330) and the archival data from other telescopes like OVRO, SMA, and Steward Observatory are collected for the same period. The multiwavelength data from all the above telescopes are used to study the flux and polarization variability, and it is discussed in this particular section. I have also presented a correlation study among different wavelengths during the outburst period (MJD 58060–MJD 58330). A single-zone emission model is chosen to perform the multiwavelength SED modeling.

3.1. Multiwavelength Light Curves

Blazar 3C 279 is known for its chaotic variability and active flaring behavior across the EM spectrum. The source was reported to be in a flaring state across the entire EM spectrum between 2017 and 2018. The multiwavelength light curve of 3C 279 during the flaring episode MJD 58060–MJD 58330 is shown in Figure 1. The first panel shows the one day binning of *Fermi*-LAT data in the energy range of 0.1–300 GeV. Our analysis shows the source was in flaring state during the end of 2017 to mid 2018. The high activity started at the end of 2017 and was followed by a flaring state defined as “Flare A.” After “Flare A,” the source was observed for around two months in a low state with small fluctuations in the flux value. 3C 279 again went to a higher state and spent around two weeks in flaring state labeled as “Flare B.” After a one month period of “Flare B,” the flux again started rising, and the source attained a full flaring state labeled as “Flare C.” The red bold vertical lines are drawn in Figure 1 corresponding to each gamma-ray flare. Just before “Flare A,” the source has been observed in a long low flux state. I have chosen a 50 day period between MJD 58060 and 58110 when the source flux is very low and constant over a long time. This period defined as “quiescent state” shown by cyan color data points in Figure 1 and separated by flaring state by a cyan color vertical line. The average flux observed during this period is $0.73 \times 10^{-6} \text{ ph cm}^{-2} \text{ s}^{-1}$.

Swift-XRT/UVOT has also monitored the source during the gamma-ray outburst. The X-rays, optical, and UV light curves are shown in panels 2, 3, and 4 of Figure 1. 3C 279 has gone through the strong X-ray flaring episode corresponding to each

gamma-ray flare. In optical and UV bands 3C 279 has shown the flaring behavior corresponding to “Flare A” and “Flare C,” while “Flare B” of the gamma-ray is missing in optical and UV because of the unavailability of UVOT observations.

3C 279 has also been monitored by Steward Observatory in optical *V* and *R* bands. In panel 5 of Figure 1, I have plotted the Steward data, and it can be seen that the source is highly variable in both the bands. “Flare A” of the gamma-ray is followed by the flare in both *V* and *R* bands. “Flare B” is observed close in time at optical (Steward Observatory) and gamma-ray, while “Flare C” is not seen in Steward Observatory because of poorly sparsed *V* and *R* band data points.

In the sixth and seventh panels of Figure 1, I have plotted the optical DoP and PA from Steward Observatory. Huge variations are seen during the flaring period. DoP varies from 4% to 22% in 12 days of span (MJD 58130–58142) and on the other hand a slow change is seen in PA from 25° to 60° .

The radio light curves from SMA and OVRO observatories at 230 and 15 GHz are shown in the last two panels of Figure 1. The radio data at 230 GHz from SMA observatory shows that the source is variable in this energy band, and high state radio flux has been noticed during “Flare A” and “Flare B.” It is observed that there are not much variations in the OVRO flux during the flaring period of gamma-ray/X-ray/optical/UV.

3.2. Variations in Gamma-Ray

In Figure 2, the gamma-ray flares are plotted separately along with the corresponding photon spectral index. “Flare A” is shown in the leftmost panel of Figure 2. The source starts showing the activity at MJD 58115 with a small rise in flux. The small fluctuations continued until the source went to the higher state, where the flux rose above the quiescent state flux value within the 10 days of time interval (MJD 58129–58140). The flux at MJD 58129.5 is $1.89 \times 10^{-6} \text{ ph cm}^{-2} \text{ s}^{-1}$ and almost after seven days the flux rose up to $22.24 \times 10^{-6} \text{ ph cm}^{-2} \text{ s}^{-1}$ at MJD 58136.5 and the photon spectral index became harder changing from 2.43 to 2.19, respectively. Just after three days from the peak, the flux started decreasing and within 10 days, it attained the low flux state at MJD 58149.5 with a flux of $1.08 \times 10^{-6} \text{ ph cm}^{-2} \text{ s}^{-1}$ and spectral index 2.31.

The middle panel of Figure 2 represents the light curve of “Flare B.” The activity was found to commence at MJD 58215 just after two months of “Flare A.” The flux started rising very slowly from MJD 58216.5 with flux $1.35 \times 10^{-6} \text{ ph cm}^{-2} \text{ s}^{-1}$ and in the span of two weeks it achieved the maximum flux value of $19.06 \times 10^{-6} \text{ ph cm}^{-2} \text{ s}^{-1}$ at MJD 58228.5. The spectral index became harder from 2.84 to 2.04. Within one day the flux dropped from $(19.06-7.49) \times 10^{-6} \text{ ph cm}^{-2} \text{ s}^{-1}$ and then the source went through small fluctuations in flux for 20 days before reaching the quiescent state. The quiescent state flux noticed at MJD 58249.5 is $1.00 \times 10^{-6} \text{ ph cm}^{-2} \text{ s}^{-1}$.

“Flare C” is shown in the rightmost panel of Figure 2. As soon as “Flare B” ends, the flux starts fluctuating again above the quiescent state flux value ($0.27 \times 10^{-6} \text{ ph cm}^{-2} \text{ s}^{-1}$) and it continues until one week and shows a little rise in flux ($3.36 \times 10^{-6} \text{ ph cm}^{-2} \text{ s}^{-1}$). After spending two days in a high flux state, the source comes back to a low flux state, and after five days it again rises to a higher flux state. The maximum flux achieved during the high flux state is $13.31 \times 10^{-6} \text{ ph cm}^{-2} \text{ s}^{-1}$ at MJD 58271.5.

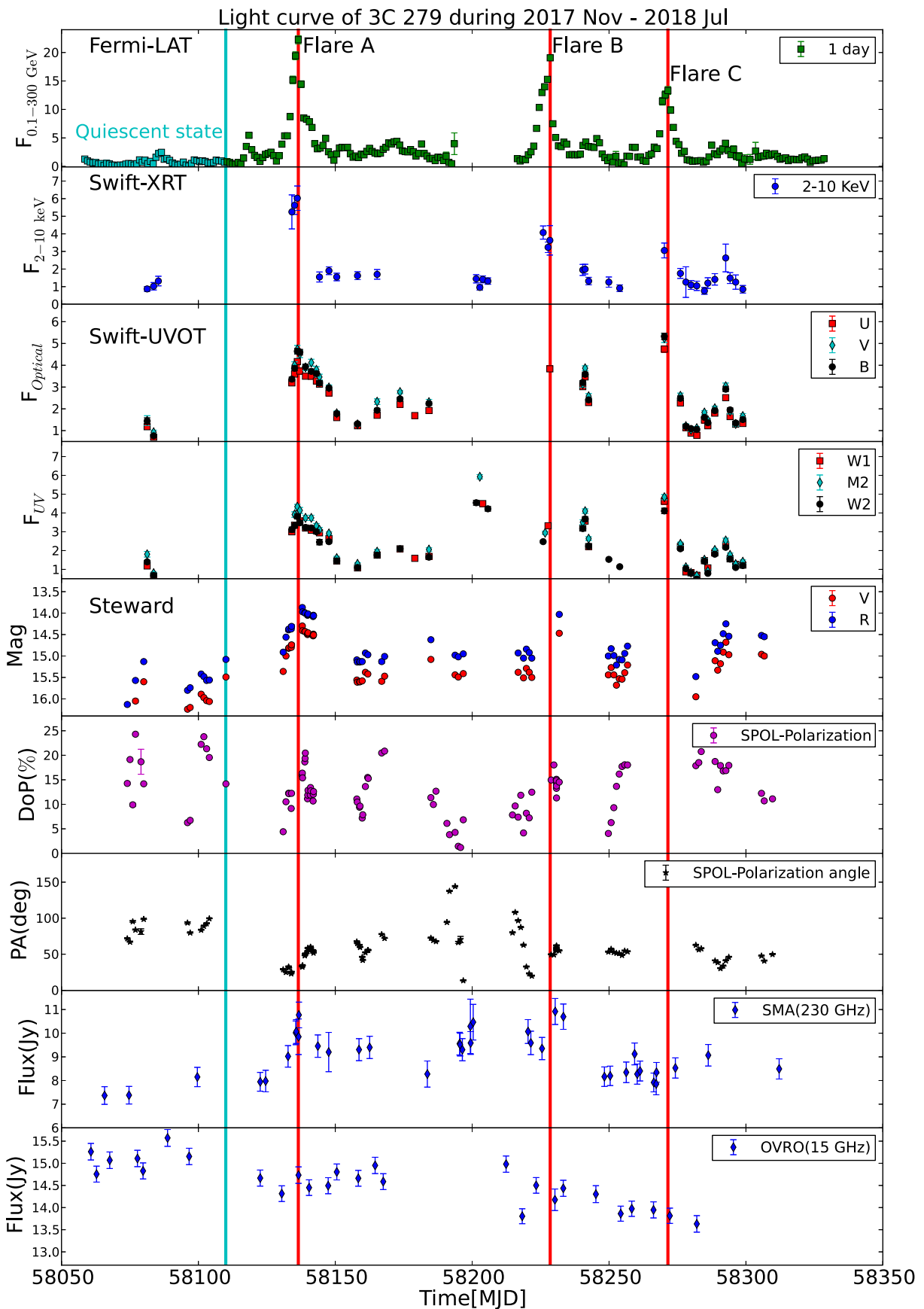


Figure 1. Multiwavelength light curve of 3C 279 from 2017 November to 2018 July. The γ -ray fluxes are presented in units of $10^{-6} \text{ ph cm}^{-2} \text{ s}^{-1}$, and X-ray/UV/optical fluxes are in units of $10^{-11} \text{ erg cm}^{-2} \text{ s}^{-1}$. The vertical cyan color line separates the quiescent state and flaring state. The red vertical lines corresponding to each gamma-ray flare are drawn to recognize the flare in all wavebands.

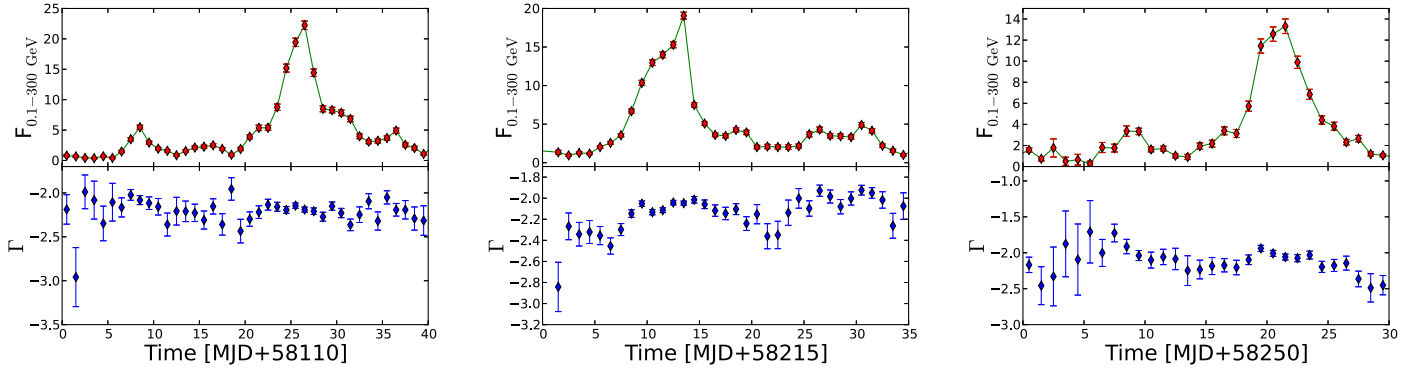


Figure 2. Gamma-ray light curve for all three flares separately with corresponding photon spectral index. The y-axis of the upper panels is in units of $10^{-6} \text{ ph cm}^{-2} \text{ s}^{-1}$.

One day bin light curves shown in Figure 2 are used to estimate the variability time, which can be defined by the following equation (Zhang et al. 1999),

$$t_{\text{var}} = \frac{F_1 + F_2}{2} \frac{t_2 - t_1}{|F_2 - F_1|} \quad (1)$$

where F_1 and F_2 are the fluxes measured at times t_1 and t_2 . The above Equation (1) is used to scan the 1 day bin light curve (Figure 2) to find the variability time. The shortest variability time is found to be order of days in all the three flares and the details are shown in Table 2. In Figure 3, the gamma-ray flux and the photon spectral index during the flaring period are plotted together along the x- and y-axes, respectively. A “harder-when-brighter” trend of source is seen here. A similar trend was also previously seen for 3C 279 by Hayashida et al. (2012, 2015), and Paliya (2015). The spectral hardening during the flaring state can predict the possibility of detection of high energy photons and consequently can shift the IC peak of the SED to higher energy. A strong correlation between spectral hardening during flare and detection of high energy photons is shown by many authors (Britto et al. 2016; Shah et al. 2019).

3.3. Variations in X-Ray

The *Swift*-XRT light curve of all the flares for 2–10 keV is shown in Figure 4 along with the photon spectral index. The observations done by *Swift*-XRT are poorly spaced, and as a result, there is no clear indication of the rising and decaying part of the flares. The maximum flux achieved during “Flare A” in X-ray is $(6.03 \pm 0.70) \times 10^{-11} \text{ erg cm}^{-2} \text{ s}^{-1}$ with spectral index 1.23 ± 0.14 . After around a two month period of “Flare A,” “Flare B” is observed in X-ray at the same time as the gamma-ray flare. The maximum flux achieved in X-ray during this period is $(4.07 \pm 0.37) \times 10^{-11} \text{ erg cm}^{-2} \text{ s}^{-1}$ and the spectral index noticed as 1.22 ± 0.11 . The last flare in X-ray, i.e., “Flare C,” is followed by small fluctuations at the end. The highest flux observed during “Flare C” is $(3.06 \pm 0.42) \times 10^{-11} \text{ erg cm}^{-2} \text{ s}^{-1}$, and the corresponding spectral index is found to be 1.35 ± 0.12 .

Figure 4 reveals “harder-when-brighter” behavior in X-ray as well, which is also reported by Hayashida et al. (2012, 2015). The average photon spectral index is estimated as 1.52 ± 0.03 , which is softer than the spectral index observed at highest flux, i.e., 1.23 ± 0.14 during “Flare A.” Most of the contribution of soft X-ray goes to synchrotron peak and the lower part of the

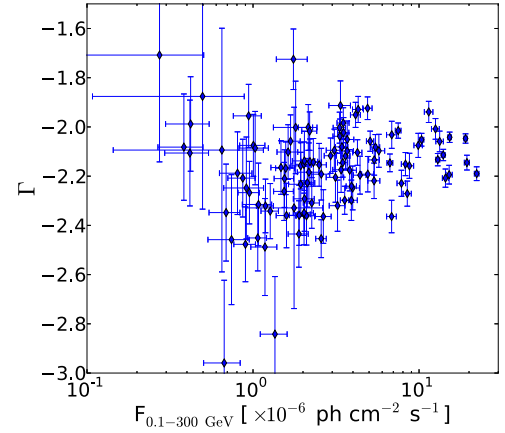


Figure 3. The gamma-ray photon spectral index corresponding to flux observed during flare shows a “harder-when-brighter” trend.

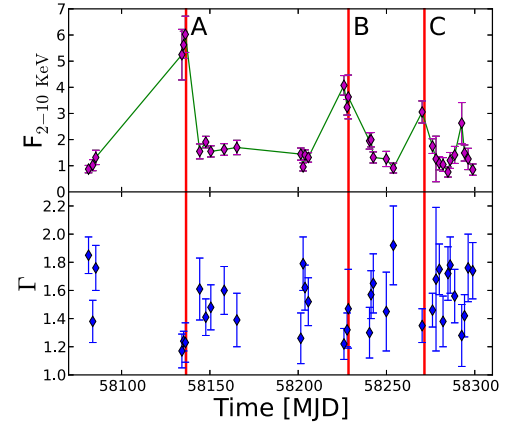


Figure 4. X-ray light curve for all the observed flares. The fluxes are in units of $1.0 \times 10^{-11} \text{ erg cm}^{-2} \text{ s}^{-1}$. Lower panel represents the corresponding photon spectral index. A “harder-when-brighter” trend is also seen here.

Table 2

Variability Time Estimated from Equation (1) for All the Different Flares

Flares	F_1	F_2	t_1	t_2	t_{var} (days)
Flare A	1.89	3.91	58129.5	58130.5	1.43 ± 0.16
Flare B	19.06	7.49	58228.5	58229.5	1.14 ± 0.03
Flare C	5.73	11.44	58268.5	58269.5	1.50 ± 0.11

Note. Fluxes F_1 and F_2 are in units of $10^{-6} \text{ ph cm}^{-2} \text{ s}^{-1}$ and t_1 and t_2 are in MJDs.

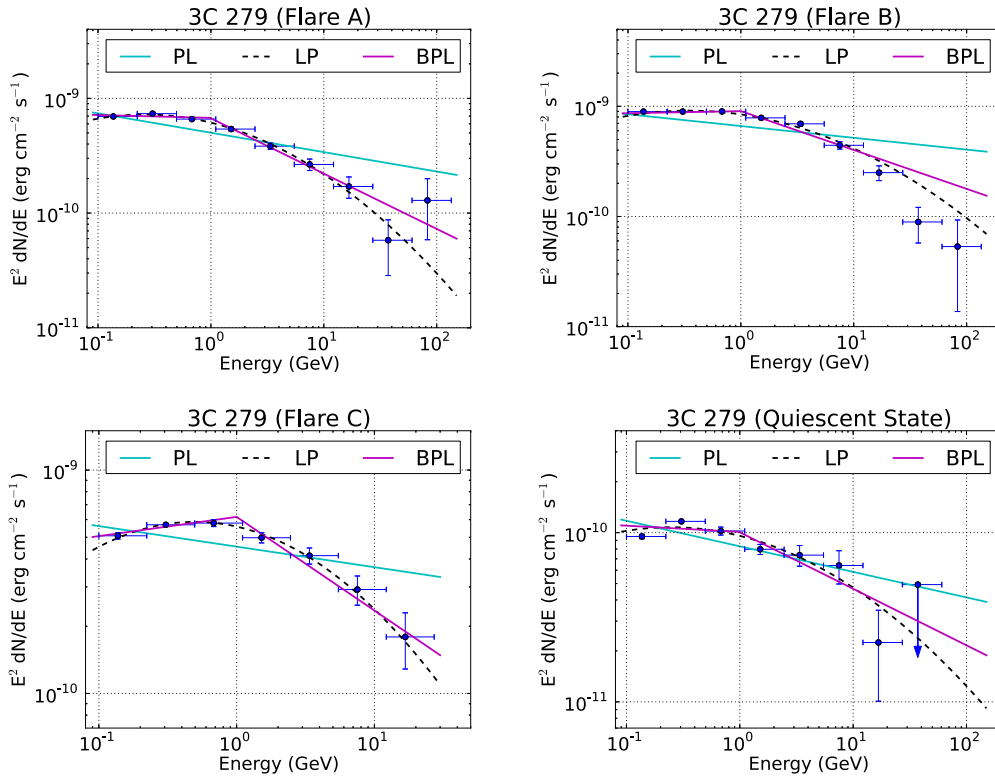


Figure 5. The gamma-ray SEDs produced for all the flares and quiescent state. The data points are fitted with three different models and the modeled parameters are shown in Table 3.

SSC/IC peak. The “harder-when-brighter” trend in X-ray can be interpreted as the increase in the SSC emission and can also shift the SSC peak toward the higher energy. Increase in the SSC/IC emission is probably due to an increase of the accretion rate.

The variability time is a tool to find out the size and location of the emission region. In the case of X-ray emission, the light curve is poorly sparsely and so cannot be used to estimate the variability time in X-ray. The location of the X-ray emission region can be estimated indirectly by the correlations study between gamma-ray and X-ray emissions. The details of the correlations study are shown in Section 3.6.

3.4. Spectral Analysis

The γ -ray SEDs have been generated for all three flares and one quiescent state between 0.1 and 300 GeV, from the likelihood analysis. The spectral data points are plotted in Figure 5, I have used three different spectral models to fit the SEDs data points. The spectral models are PL, Log-parabola (LP), and simple broken power-law (BPL), and corresponding expressions are given in Prince et al. (2018). The presence or absence of curvature in the gamma-ray SED plays a crucial role in constraining the location of the emission region. A break in the gamma-ray spectrum is expected when the emission region is within the broad line region (BLR), because of photon-photon pair production. An earlier study by Liu & Bai (2006) has shown that the BLR region is opaque to photons of energy >20 GeV, and as a result, a curvature or break can be seen in the gamma-ray spectrum above 20 GeV. The curvature in the gamma-ray spectrum can be justified by estimating the TS_{curve} . According to Nolan et al. (2012) the TS_{curve} can be defined as $TS_{\text{curve}} = 2(\log L(\text{LP}/\text{BPL}) - \log L(\text{PL}))$, where L represents

the likelihood function. The model parameters and the value of TS_{curve} are mentioned in Table 3. The model which has a large positive value of TS_{curve} is considered as the best fit to the SEDs data points and it suggests the presence of a spectral cutoff. From Table 3, it is very clear that the LP spectral model better explains the gamma-ray SED data. I have also noticed that the break energy found in BPL fit is constant irrespective of the different flares. This finding is also consistent with the previous study on this source, by Paliya (2015), and on 3C 454.3 by Abdo et al. (2011). There is also an alternative way to explain this curvature/cut-off. A cutoff in the energy spectrum can also occur when there is already a cutoff in the energy distributions of the particles.

A strong break is seen in the gamma-ray spectrum while fitting with BPL; a similar break has also been seen before for other FSRQs like 3C 454.3 by Abdo et al. (2011) and also for 3C 279 during flares of 2014 and 2015 (Paliya 2015; Paliya et al. 2015b). In Table 3, during all the flares the BPL photon index (Γ_1) before the break ($E_{\text{break}} = 1$ GeV) is ≤ 2 , which suggests an increasing slope, and after the break the photon spectral index (Γ_2) is ≥ 2 , indicating a falling spectrum. We know that the gamma-ray energy spectrum is governed by IC scattering and my result shows it peaks around 1 GeV, which lies in the energy range of LAT (0.1–300 GeV). Since the break energy is almost constant for all the flares, it is possible that the observed shape is a reminiscence of the electron energy distribution of the emitting electrons.

3.5. Fractional Variability (F_{var})

Blazars are a particular class of AGN that show strong chaotic variability at all frequencies. The variability is more evident during the flaring period and the flare profiles mostly

Table 3
Parameters Obtained from the Spectral Analysis Fit, for the Different Models PL, LP, and BPL, by using the Likelihood Analysis Method

Power Law (PL)						
Activity	$F_{0.1-300 \text{ GeV}}$ ($10^{-6} \text{ ph cm}^{-2} \text{ s}^{-1}$)	Γ			TS	TS _{curve}
Quiescent state	0.67 ± 0.02	2.15 ± 0.03	3625.24	...
Flare A	4.42 ± 0.05	2.17 ± 0.92	35533.08	...
Flare B	5.59 ± 0.05	2.11 ± 0.01	67293.68	...
Flare C	3.47 ± 0.06	2.09 ± 0.02	15163.31	...
Log-parabola (LP)						
		α	β			
Quiescent state	0.64 ± 0.03	2.04 ± 0.04	0.06 ± 0.02	...	3653.27	28.03
Flare A	4.24 ± 0.05	2.05 ± 0.02	0.090 ± 0.008	...	35759.77	226.69
Flare B	5.39 ± 0.05	1.99 ± 0.01	0.072 ± 0.006	...	67311.92	18.24
Flare C	3.26 ± 0.07	1.93 ± 0.02	0.10 ± 0.01	...	15282.46	119.15
Broken Power Law (BPL)						
		Γ_1	Γ_2	E_{break}		
Quiescent state	0.65 ± 0.03	2.04 ± 0.05	2.33 ± 0.08	0.98 ± 0.17	3633.04	7.8
Flare A	4.27 ± 0.05	2.02 ± 0.02	2.48 ± 0.03	0.98 ± 0.05	35750.45	217.37
Flare B	5.42 ± 0.05	1.98 ± 0.01	2.35 ± 0.02	1.00 ± 0.03	67309.47	15.79
Flare C	3.30 ± 0.07	1.91 ± 0.03	2.42 ± 0.05	1.00 ± 0.06	15263.59	100.28

Note. TS_{curve} is estimated with respect to the TS value of the PL fit.

Table 4
Fractional Variability in Various Wavebands Are Estimated for the Time Interval MJD 57980–58120

Waveband	F_{var}	err(F_{var})
γ -ray	1.201	0.008
X-ray	0.660	0.035
U	0.524	0.008
B	0.520	0.006
V	0.509	0.008
W1	0.548	0.008
M2	0.580	0.007
W2	0.557	0.007
OVRO (15 GHz)	0.032	0.002
SMA (230 GHz)	0.089	0.010

depend on the particle injection, particle acceleration, and energy dissipation in the jets of blazars. The variability amplitude can be estimated by measuring all kinds of jet parameters like the magnetic field in the jets, viewing angle of the jet, particle density inside the jet, and finally the efficiency of the acceleration process involved within the jet. The challenge to determine the variability amplitude across the energy band requires a good quality of data. 3C 279 is a well-observed source across the EM spectrum, and that makes it possible to estimate the variability amplitude. The fractional root mean square variability parameter (F_{var}) is a tool to determine the variability amplitude and that is introduced by Edelson & Malkan (1987) and Edelson et al. (1990). The relation given in Vaughan et al. (2003) is used to determine the fractional variability (F_{var}),

$$F_{\text{var}} = \sqrt{\frac{S^2 - \sigma^2}{r^2}} \quad (2)$$

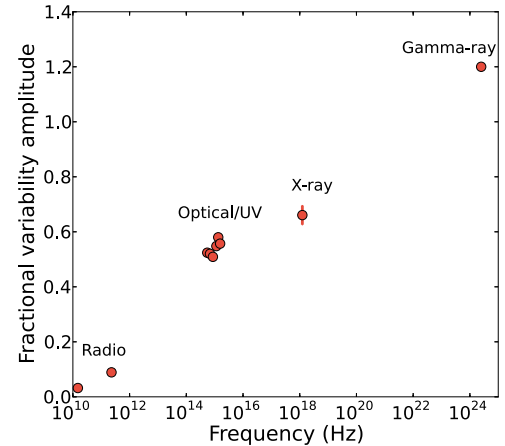


Figure 6. Fractional variability for various wavebands are plotted with respect to their frequency.

$$\text{err}(F_{\text{var}}) = \sqrt{\left(\sqrt{\frac{1}{2N}} \cdot \frac{\sigma^2}{r^2 F_{\text{var}}}\right)^2 + \left(\sqrt{\frac{\sigma^2}{N}} \cdot \frac{1}{r}\right)^2} \quad (3)$$

where $\sigma_{\text{XS}}^2 = S^2 - \sigma^2$, is called excess variance, S^2 is the sample variance, σ^2 is the mean square uncertainties of each observation, and r is the sample mean.

The fractional variability estimated across the EM spectrum is shown in Figure 6, and the values are presented in Table 4. It is seen that the source variability is more than 100% in γ -ray, followed by X-ray at more than 60%, and then followed by UV and optical, where the source variability is more than 50%. In radio at 15 and 230 GHz, the source is much less variable (less than 10%) during this particular gamma-ray flaring period. The F_{var} is 1.201 in γ -ray, 0.580 in UVM2-band, 0.520 in optical U-band and 0.032 in radio at 15 GHz, and 0.089 at 230 GHz. It

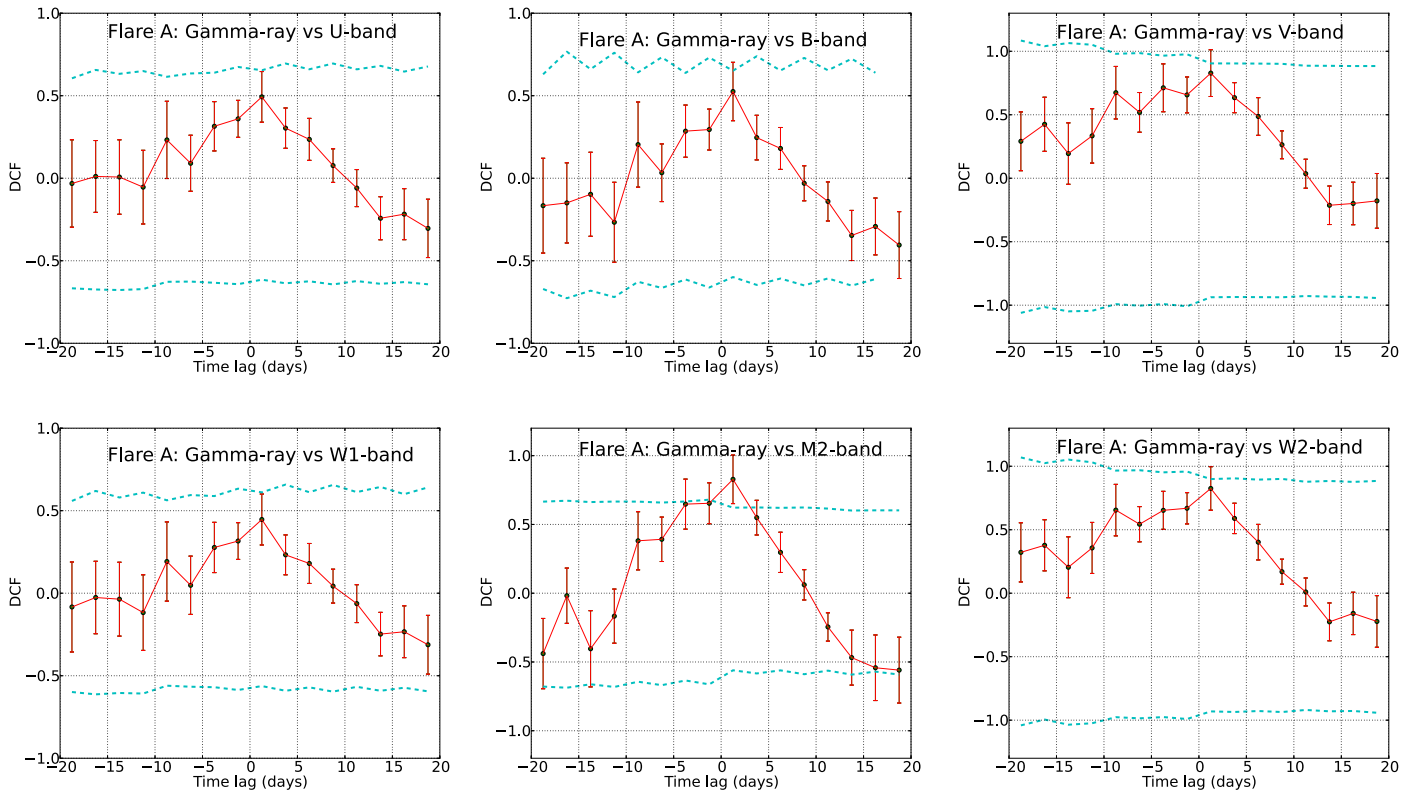


Figure 7. DCFs shown for “Flare A” for all the possible combinations: γ vs. *Swift-U, B, V, W1, M2, W2* bands. The significance shown in cyan color is 95%.

is found that F_{var} is increasing with energy, suggesting that a large number of particles are injected in the jet, resulting in high energy emission. Similar behavior of fractional variability is also seen for other FSRQs like Ton 599 by Prince (2019), where he found a trend of large fractional variability toward higher energies. This is not always the case, and an opposite trend was also noticed in the past. An opposite trend is reported by Bonning et al. (2009), where variability amplitudes decrease toward shorter wavelengths (IR, optical, and UV), which suggests the presence of steady thermal emission from the accretion disk.

3.6. Correlation Studies

In Figure 1, all the light curves are plotted together, and the visual inspection suggests that the flares in γ -ray, X-ray, optical, and UV band are mostly correlated. The radio light curve at 15 GHz does not show any flare for this particular period, while the light curve at 230 GHz shows a rise in flux corresponding to “Flare A” and “Flare B.” The gamma-ray “Flare C” detected in X-rays, and optical/UV have not been seen in radio at 230 GHz. The cross-correlation study of flux variations in different energy bands is presented in this section. The correlation study helps to reveal the location of the emission region in different energy bands with respect to each other. A strong and good correlation between two energy emissions indicates their cospatial origin. A positive and negative time lag between two energy bands with strong correlation coefficient suggests the different emission region for different waveband emissions and the time lag can be used to estimate the separation between them (Fuhrmann et al. 2014). The correlation study is done by using the *discrete correlations function* (DCF) formulated by Edelson (1988). When the two light curves, say LC1 and LC2, are correlated then a positive time lag between these two light curves implies

that LC1 is leading LC2, and a negative time lag means the opposite. The results of DCFs are shown in Figures 7–9 for “Flare A” and “Flare C,” for various waveband combinations.

A cross-correlation study between two light curves (different energy band) by DCF needs sufficient data points in each light curve. “Flare B” fails to fulfill this criteria since it has good quality data points only in the gamma-ray light curve. It is therefore not possible to cross-correlate two different energy bands for “Flare B.” Significant correlation has been noticed between gamma-ray and optical band (*U, B, and V*) emissions with zero time lag (within the time bin 2.5 days). The correlation coefficient for “Flare A” is found to be 0.50 ± 0.15 , 0.53 ± 0.17 , 0.83 ± 0.18 and for “Flare C” it is 0.92 ± 0.44 , 0.93 ± 0.44 , 0.91 ± 0.44 in *U, B, and V* bands, respectively. The cross-correlation between gamma-ray and UV band (*W1, M2, and W2*) emission are very similar to the gamma-ray versus optical band emission. The correlation coefficients for “Flare A” and “Flare C” are 0.45 ± 0.15 , 0.83 ± 0.17 , 0.82 ± 0.17 , and 0.92 ± 0.44 , 0.90 ± 0.43 , 0.89 ± 0.43 in *W1, M2, and W2* bands, respectively. A strong correlation with zero time lag is observed between gamma-ray and X-ray emission for 3C 279. To the author’s knowledge this is the first time the source has shown strong correlation with zero time lag between gamma-ray and X-ray. The value of correlation coefficients for “Flare A” and “Flare C” are noted as 0.87 ± 0.16 and 0.97 ± 0.36 , respectively, at zero time lag (within the time bin). The significances of the DCF peaks are also estimated by simulating the 1000 gamma-ray light curves. To simulate the gamma-ray light curves, I have used the method mentioned in Emmanoulopoulos et al. (2013). Further, I cross-correlate the simulated gamma-ray light curves with the observed light curves in different wavebands and finally a DCF distribution with time lag is calculated. At each time lag 95%

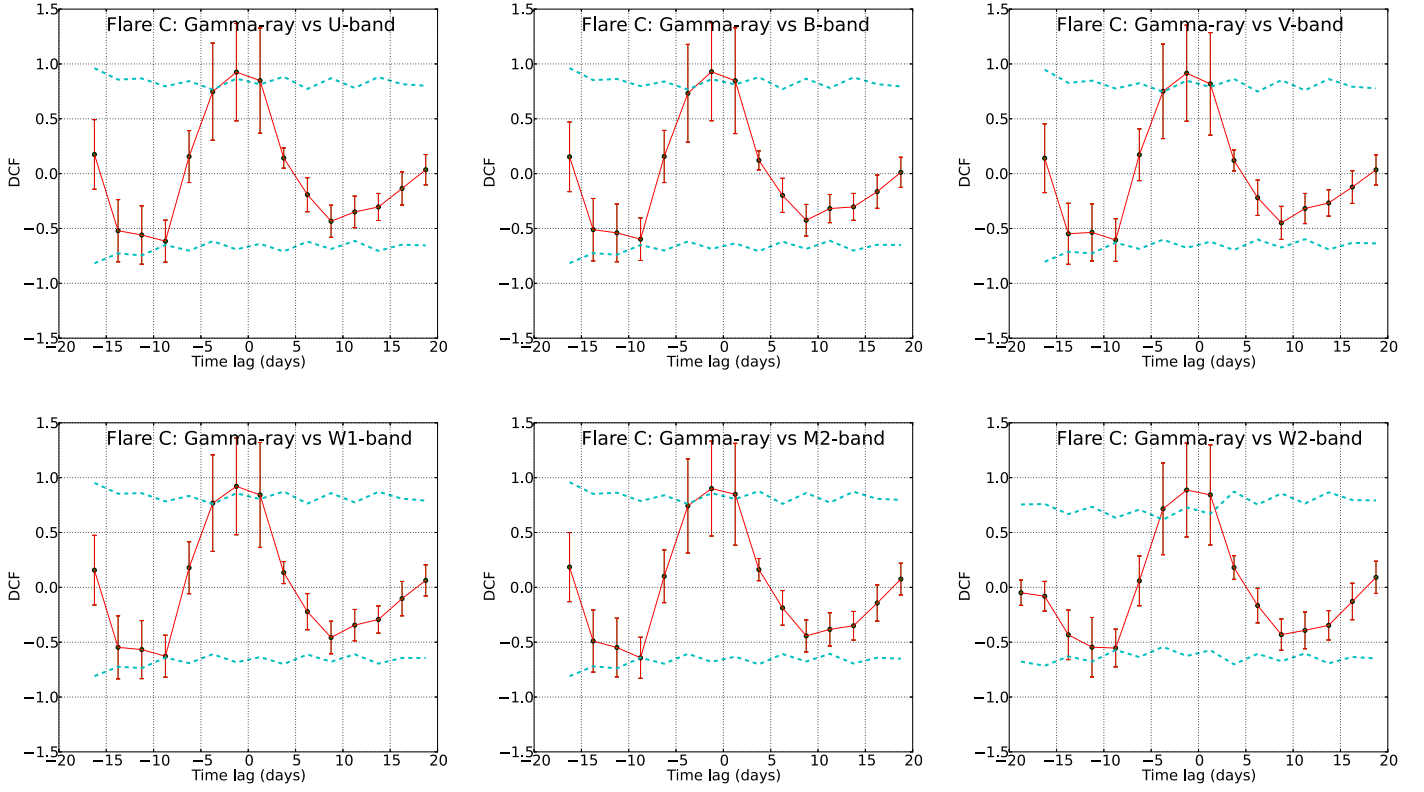


Figure 8. DCF shown for “Flare C” for all the possible combinations: γ vs. Swift-*U*, *B*, *V*, *W1*, *M2*, *W2* bands. The significance shown in cyan color is 95%.

significance was calculated, which is shown in cyan color in Figures 7, 8, and 9.

4. Modeling the Multiwavelength SED

The simultaneous observation of 3C 279 in different energy bands during its 2017–2018 flaring period provides an opportunity to gain further insight into its multiwavelength properties. In this work, theoretical modeling of the observed SED is done using the publicly available code GAMERA³ (Hahn 2015) which solves the time-dependent transport equation and calculates the propagated electron distribution.

This electron spectrum was used as an input to estimate the synchrotron, synchrotron self-Compton (SSC), and IC emissions. The transport equation used in the code is the following,

$$\frac{\partial N(E, t)}{\partial t} = Q(E, t) - \frac{\partial}{\partial E}(b(E, t)N(E, t)) \quad (4)$$

where $Q(E, t)$ is the injected electron spectrum, and $N(E, t)$ is the spectrum achieved after the radiative loss. The radiative loss due to synchrotron, SSC, and IC is represented by $b(E, t)$. GAMERA takes care of the IC in the Klein–Nishina regime from Blumenthal & Gould (1970). The transport equation does not have the diffusive loss term as it is insignificant compared to the radiative loss of the electrons. The LP spectral model is chosen as the input injected electron spectrum, motivated from the gamma-ray spectral analysis. To model the multiwavelength SEDs, my model considers a single spherical emitting zone or blob which is moving down the jet along the jet axis with a Lorentz factor, Γ , and Doppler factor, δ . The external

photon field required for external Compton emission is believed to be dominated by the BLR photons, particularly in an FSRQ like 3C 279. The BLR photon density in the comoving frame is given by,

$$U'_{\text{BLR}} = \frac{\Gamma^2 \eta_{\text{BLR}} L_{\text{disk}}}{4\pi c R_{\text{BLR}}^2} \quad (5)$$

where the η_{BLR} represents the fraction of disk emission processed in BLR, I assume it to be typically 2% (Pittori et al. 2018), R_{BLR} is the size of the BLR, L_{disk} denotes the disk luminosity, and c is the speed of light in vacuum. The photon energy density in BLR is only a fraction $\eta_{\text{BLR}} \sim 0.02(2\%)$ of the disk photon energy density.

The size of the BLR can be written as $R_{\text{BLR}} = 10^{17} L_{d,45}^{1/2}$ (Ghisellini & Tavecchio 2009), where $L_{d,45}$ is the accretion disk luminosity in units of $10^{45} \text{ erg s}^{-1}$. For $L_{\text{disk}} = 2 \times 10^{45} \text{ erg s}^{-1}$ (Pian et al. 1999), the size of BLR is estimated to be $R_{\text{BLR}} = 1.414 \times 10^{17} \text{ cm}$.

The minimum Doppler factor (δ_{min}) during the flare can be estimated from the $\gamma\gamma$ opacity arguments and by estimating the highest energy photon. The minimum Doppler factor can be calculated as (Doni & Ghisellini 1995; Ackermann et al. 2010),

$$\delta_{\text{min}} \cong \left[\frac{\sigma_{\text{T}} d_L^2 (1+z)^2 f_x \epsilon}{4 t_{\text{var}} m_e c^4} \right]^{1/6} \quad (6)$$

which assumes that the optical depth of a photon ($\tau_{\gamma\gamma}$) with energy $\epsilon = E/m_e c^2$ to the $\gamma\gamma$ interaction is 1. The luminosity distance is denoted as $d_L (=3.1 \text{ Gpc})$, σ_{T} is the Thomson scattering cross section, E is the highest photon energy detected during the flare, t_{var} is the variability time, and f_x is the X-ray

³ http://libgamera.github.io/GAMERA/docs/main_page.html

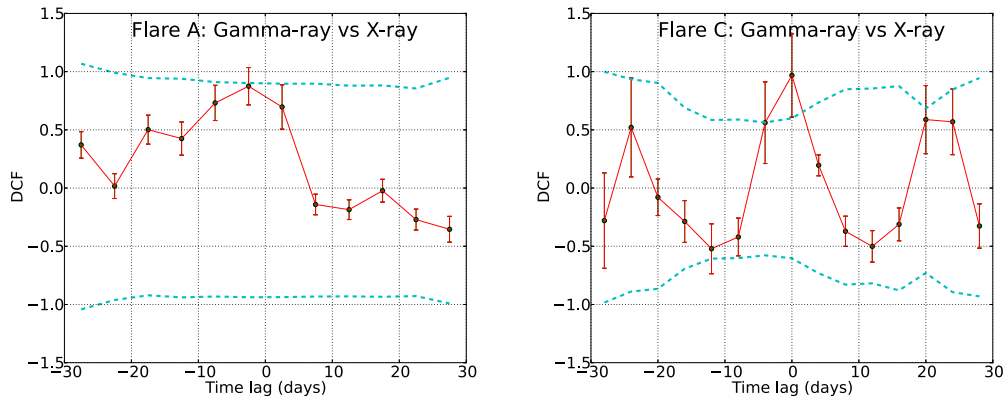


Figure 9. Gamma-ray vs. X-ray DCF are shown for “Flare A” and “Flare C.” The significance shown in cyan color is 95%.

flux in 0.3–10 keV. Here, the values of E , f_x , and t_{var} are estimated around the same time period and the values are found to be 27 GeV at MJD 58228.45, 3.63×10^{-11} erg cm $^{-2}$ s $^{-1}$ at MJD 58228.38, and 1.14 days at MJD 58228.50, respectively. The minimum Doppler factor is found to be $\delta_{\text{min}} = 10.7$. The location of the gamma-ray emission region can be estimated by assuming the bulk Lorentz factor $\Gamma = \delta_{\text{min}} = 10.7$, then the location can be defined as $d \sim 2 c \Gamma^2 t_{\text{var}} / (1 + z)$. It is found that the gamma-ray emission region is located at a distance of 4.40×10^{17} cm from the central SMBH down the jet. This value is comparable to the size of the BLR and hence I concluded that during the emission of high energy photon (27 GeV) the gamma-ray emitting region must have been located at the outer boundary of the BLR.

I have also considered the contribution of the accretion disk photons in the EC emission. The photon energy density in the comoving frame is defined as (Dermer & Menon 2009),

$$U'_{\text{disk}} = \frac{0.207 R_g l_{\text{Edd}} L_{\text{Edd}}}{\pi c z^3 \Gamma^2} \quad (7)$$

where R_g is known as gravitational radius, and $l_{\text{Edd}} = L_{\text{disk}}/L_{\text{Edd}}$ is the Eddington ratio. Here z represents the distance of the blob from the SMBH, which is estimated to be 4.40×10^{17} cm. For black hole mass $M_{\text{BH}} = 2.51 \times 10^8 M_{\odot}$ (Wu et al. 2018), the gravitational radius is found to be $R_g = 3.72 \times 10^{13}$ cm. In this study, I have not considered dusty torus as an external target photon field since there is no observational evidence. However, the contribution of NIR/optical/UV photons emitted by disk and dusty torus based clouds irradiated by a spine-sheath jet could be important (Finke 2016; Breiding et al. 2018; Gaur et al. 2018) for the EC emission in some cases.

There are numbers of parameters that GAMERA uses as an input to model the multiwavelength emissions. The spectral index (α , β), minimum and maximum (γ_{min} , γ_{max}) energies, magnetic field inside the blob (B), and luminosity in injected electrons are the parameters that have been optimized to obtain the best model fit to the SEDs. The BLR photon density (U'_{BLR}), BLR temperature = 10^4 K (Peterson 2006), accretion disk photon density (U'_{disk}), and disk temperature = 2.6×10^6 K (Dermer & Menon 2009) are kept fixed while modeling the SEDs.

The size of the blob can also be estimated by using the variability time and the minimum Doppler factor by the

relation,

$$R \leq c t_{\text{var}} \delta (1 + z)^{-1} \quad (8)$$

where t_{var} is the observed flux variability time (1.14 days). The size of the emitting blob is estimated to be $R = 2.1 \times 10^{16}$ cm. However, during the SED modeling Doppler factor and the size of the blob are optimized to best-fit value.

A successful SED modeling is performed for all three flares and one quiescent state. The best-fit model parameters are shown in Table 5. The multiwavelength SEDs modeled with GAMERA are presented in Figure 10. The low energy synchrotron peak is constrained by the optical and UV emission and the high energy Compton peak by gamma-ray data points. The X-ray emission observed by *Swift*-XRT constrains the SSC peak. More magnetic field value is needed to explain the optical/UV emission in quiescent state, which suggests that the synchrotron process is more dominant here compared to the flaring state. The maximum electron energy found during all of the states is very consistent; though, it is a little higher during the flaring state. The total jet power is estimated by the following relation,

$$P_{\text{jet}} = \pi \Gamma^2 r^2 c (U_e + U_B + U_p) \quad (9)$$

where Γ is the Lorentz factor, and r is the size of the blob. The energy density in electrons, magnetic field, and cold protons are represented by U_e , U_B , and U_p . Here the jet composition consists of an equal number of nonthermal electrons and cold protons. The calculated jet powers in all components are shown in Table 5. The jet power is calculated for $\Gamma = 15.5$ (Jorstad et al. 2005) and $r = 4.64 \times 10^{16}$ cm. It is found that the magnetic field has more jet power during the quiescent state compared to the flares. However, the jet power required in electrons and protons is much higher in the case of the flaring state compared to the quiescent state.

The previous study on flares of 3C 279 suggest that most of the time the emission region is located outside the BLR (Dermer et al. 2014; Yan et al. 2015; Vittorini et al. 2017). However, the brightest flare of 3C 279 during 2015 June reported by Paliya (2015), demands a compact emission region with high photon density and such regions cannot be far from the central source. All earlier studies on this flare (2015 June) (Hayashida et al. 2015; Ackermann et al. 2016; Pittori et al. 2018) found the emission region to be located within or at the boundary of the BLR. Here, in this study too, a similar result is

Table 5
Results of Fitted Multiwavelength SEDs Shown in Figure 10

Activity	Parameters	Symbol	Values	Activity Period (days)
	BLR temperature	T'_{blr}	1×10^4 K	
	BLR photon density	U'_{blr}	$6.377 \text{ erg cm}^{-3}$	
	Disk temperature	T'_{disk}	2.6×10^6 K	
	Disk photon density	U'_{disk}	$7.9 \times 10^{-7} \text{ erg cm}^{-3}$	
	Size of the emission region	R	4.64×10^{16} cm	
	Doppler factor of emission region	δ	24.1	
	Lorentz factor of emission region	Γ	15.5	
Flare A	Min Lorentz factor of injected electrons	γ_{min}	8.0	
	Max Lorentz factor of injected electrons	γ_{max}	1.5×10^4	
	Spectral index of injected electron spectrum (LP)	α	1.7	
	Curvature parameter of LP electron spectrum	β	0.15	
	magnetic field in emission region	B	2.8 G	40
	jet power in electrons	P_e	$1.88 \times 10^{45} \text{ erg s}^{-1}$	
	jet power in magnetic field	P_B	$1.52 \times 10^{46} \text{ erg s}^{-1}$	
	jet power in cold protons	P_p	$1.87 \times 10^{46} \text{ erg s}^{-1}$	
Flare B	Min Lorentz factor of injected electrons	γ_{min}	10.0	
	Max Lorentz factor of injected electrons	γ_{max}	1.7×10^4	
	Spectral index of injected electron spectrum (LP)	α	1.7	
	Curvature parameter of LP electron spectrum	β	0.12	
	magnetic field in emission region	B	2.5 G	35
	jet power in electrons	P_e	$2.42 \times 10^{45} \text{ erg s}^{-1}$	
	jet power in magnetic field	P_B	$1.21 \times 10^{46} \text{ erg s}^{-1}$	
	jet power in cold protons	P_p	$2.24 \times 10^{46} \text{ erg s}^{-1}$	
Flare C	Min Lorentz factor of injected electrons	γ_{min}	8.0	
	Max Lorentz factor of injected electrons	γ_{max}	1.5×10^4	
	Spectral index of injected electron spectrum (LP)	α	1.7	
	Curvature parameter of LP electron spectrum	β	0.1	
	magnetic field in emission region	B	2.4 G	30
	jet power in electrons	P_e	$1.13 \times 10^{45} \text{ erg s}^{-1}$	
	jet power in magnetic field	P_B	$1.12 \times 10^{46} \text{ erg s}^{-1}$	
	jet power in cold protons	P_p	$1.56 \times 10^{46} \text{ erg s}^{-1}$	
Quiescent state	Min Lorentz factor of injected electrons	γ_{min}	4.0	
	Max Lorentz factor of injected electrons	γ_{max}	1.2×10^4	
	Spectral index of injected electron spectrum (LP)	α	1.7	
	Curvature parameter of LP electron spectrum	β	0.08	
	magnetic field in emission region	B	4.2 G	50
	jet power in electrons	P_e	$2.56 \times 10^{44} \text{ erg s}^{-1}$	
	jet power in magnetic field	P_B	$3.42 \times 10^{46} \text{ erg s}^{-1}$	
	jet power in cold protons	P_p	$7.17 \times 10^{45} \text{ erg s}^{-1}$	

Note. An LP model is used as electron injected spectrum which is defined as $dN/dE = N_0(E/E_0)^{(-\alpha-\beta*\log(E/E_0))}$, where E_0 is chosen as 90 MeV.

obtained. A compact emission region can be inferred, which is located within the boundary of the BLR.

The 2018 January flare of 3C 279 was also studied by Shah et al. (2019), where they have chosen BLR and IR photons as the target photons to describe the multiwavelength SEDs. They concluded that both cases can explain the broadband SEDs of various flaring states. However, the parameters found for EC/IR are more acceptable than for the EC/BLR process. Two-zone leptonic and single-zone lepto-hadronic SED modeling are performed by Paliya et al. (2015a) to describe the broadband SEDs of 3C 279 during the flare of 2013 December. However, my result shows that the single emission zone is enough to explain the broadband SEDs.

3C 279 was studied by Hayashida et al. (2012) using the broadband data from radio to gamma-ray for the first two years (2008–2010) of *Fermi* operation. They found a lag of 10 days between optical and gamma-ray emission during the flaring episode. However, they also argue that the X-ray emission does not correlate with optical or gamma-ray emission. On the other hand, my study exhibits a good correlation between optical, X-ray, and gamma-ray emission. They also plotted the optical polarization (degree and angle) along with the gamma-ray flare and found a huge swing in the PA corresponding to the gamma-ray flare (Period D). During the SED modeling, they constrained the location of the emission region based on the observed change in the optical PA. A huge swing in the PA can

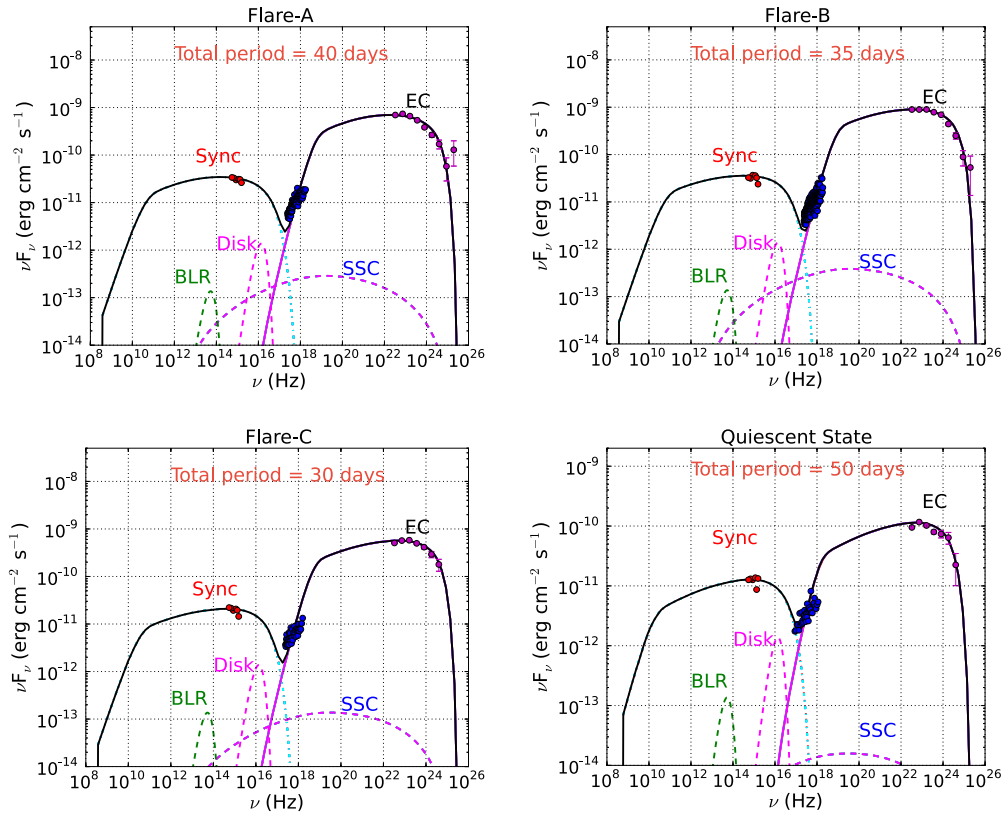


Figure 10. Multiwavelength SEDs of all the flares and one quiescent state are presented. The optimized model parameters are shown in Table 5.

be interpreted as the precession in the jet, which allows the arbitrary location of the emission region within the BLR. My study also shows a huge variation in the optical PA during the flaring episode (“Flare A” and “Flare B”). Considering the PA swing is caused by the precession of the jet, I have chosen the single emission zone within the boundary of the BLR, to model the broadband SED, which is also supported by the value estimated from the variability time.

Comparing the SEDs corresponding to quiescent and flaring states, I observed that the flux has increased during flares across the EM spectrum (Figure 10). The major flux change is observed in gamma-ray band between quiescent and flaring states. However, the change in the gamma-ray flux among the different flares (A, B, and C) is small. A relatively lesser flux change is observed in optical/UV and X-ray bands among all the states. I have varied a few parameters to explain these changes and the parameters are magnetic field, and minimum and maximum energy of electrons. I found that almost 10 times more jet power in electrons is required to explain the gamma-ray flux observed during flares compared to the quiescent state.

5. Summary

Fermi-LAT data was collected from 2017 November to 2018 July and three bright flares were observed. To differentiate them from each other the flares have been named as “Flare A,” “Flare B,” and “Flare C.” A long low flux states period was observed just before “Flare A.” This low flux states period is defined as quiescent state and a time period of 50 days is chosen to represent it. A simultaneous observation in X-ray and optical/UV was also done by the *Swift*-XRT/UVOT telescope. The archival data from the Steward observatory for optical V and R bands has also been collected for the whole period, and a

huge variation is seen in the DoP and PA. The archival radio data from OVRO and SMA are also collected for the entire flaring period.

The day-scale variability has been seen in the one day bin light curve, which constrains the size of the emission region to 2.1×10^{16} cm. The emission region is located at a distance of 4.40×10^{17} cm, which lies at the boundary of the BLR ($R_{\text{BLR}} = 1.414 \times 10^{17}$ cm). A “harder-when-brighter” trend was also observed in both gamma-ray and X-ray, which predicts detection of a high energy photon during the high state.

The gamma-ray spectral data points are fitted with three different spectral models PL, LP, and BPL. The TS_{curve} obtained for all the fits suggests that LP is the best model to describe the gamma-ray photon spectrum. Further, I have estimated the fractional variability among different wavebands, and it is observed that the fractional variability is increasing toward the higher energy.

A discrete cross-correlation (DCF) study has been performed to find out the possible correlation in the emission from various wavebands. The results show a good and strong correlation in all possible combinations like gamma-ray versus optical/UV, and gamma-ray versus X-rays. To the author’s knowledge this is the first time that a strong correlation with zero time lag between gamma-ray, X-ray, and optical/UV has been seen for 3C 279. A strong correlation and zero time lag between optical/UV, X-ray, and gamma-ray emissions suggest their cospatial origin. This outcome provides an impetus to choose a single emission zone to explain the multiwavelength emission in SED modeling. *GAMERA* is used to model the multi-wavelength emission, and the parameters like magnetic field, injected electron spectrum, and minimum and maximum

energy of injected electrons have been optimized to get a good fit to the SEDs data points. So this study suggests that a single-zone model can also be good enough to explain the multiwaveband emissions from one of the brightest *Fermi* blazars called 3C 279.

This work has made use of public *Fermi* data obtained from FSSC. This research has also made use of XRT data analysis software (XRTDAS) developed by ASI science data center, Italy. Archival data from the Steward observatory is used in this research. This research has made use of radio data from OVRO 40 m monitoring program (Richards et al. 2011) which is supported in part by NASA grants NNX08AW31G, NNX11A043G, and NNX14AQ89G and NSF grants AST-0808050 and AST-1109911. The archival data from the Submillimeter Array observatory has also been used in this study (Gurwell et al. 2007). The Submillimeter Array is a joint project between the Smithsonian Astrophysical Observatory and the Academia Sinica Institute of Astronomy and Astrophysics and is funded by the Smithsonian Institution and the Academia Sinica. R.P. thanks Saikat, Manami, and Gunjan for manuscript reading and Arkadipta for helpful discussions regarding DCF.

ORCID iDs

Raj Prince  <https://orcid.org/0000-0002-1173-7310>

References

- Abdo, A. A., Ackermann, M., Agudo, I., et al. 2010, *ApJ*, **721**, 1425
- Abdo, A. A., Ackermann, M., Ajello, M., et al. 2011, *ApJL*, **733**, L26
- Ackermann, M., Anantua, R., Asano, K., et al. 2016, *ApJL*, **824**, L20
- Ackermann, M., Asano, K., Atwood, W. B., et al. 2010, *ApJ*, **716**, 1178
- Aharonian, F., Akhperjanian, A. G., Bazer-Bachi, A., et al. 2007, *ApJL*, **664**, L71
- Alexander, T. 1997, in *Astronomical Time Ser.*, ed. D. Maoz, A. Sternberg, & E. M. Leibowitz (Dordrecht: Kluwer), 163
- Alexander, T. 2013, arXiv:1302.1508
- Atwood, W. B., Abdo, A. A., Ackermann, M., et al. 2009, *ApJ*, **697**, 1071
- Blumenthal, R., & Gould, G. 1970, *RvMP*, **42**, 237
- Bonning, E. W., Bailyn, C., Urry, C. M., et al. 2009, *ApJL*, **697**, L81
- Breeveld, A. A., Landsman, W., Holland, S. T., et al. 2011, in *AIP Conf. Proc.* 1358, *Gamma Ray Bursts 2010*, ed. J. E. McEnery, J. L. Racusin, & N. Gehrels, 373
- Breiding, P., Georganopoulos, M., & Meyer, E. 2018, *ApJ*, **853**, 19
- Britto, R. J., Bottacini, E., Lott, B., et al. 2016, *ApJ*, **830**, 162
- Chatterjee, R., Jorstad, S. G., Marscher, A. P., et al. 2008, *ApJ*, **689**, 79
- Cohen, D. P., Romani, R. W., Filippenko, A. V., et al. 2014, *ApJ*, **797**, 137
- Dermer, C. D., Cerruti, M., Lott, B., Boisson, C., & Zech, A. 2014, *ApJ*, **782**, 82
- Dermer, C. D., & Menon, G. 2009, *High Energy Radiation from Black Holes* (Princeton: NJ: Princeton Univ. Press)
- Dermer, C. D., Schlickeiser, R., & Mastichiadis, A. 1992, *A&A*, **256**, L27
- Dondi, L., & Ghisellini, G. 1995, *MNRAS*, **273**, 583
- Edelson, R. A., & Krolik, J. H. 1988, *ApJ*, **333**, 646
- Edelson, R. A., Krolik, J. H., & Pike, G. F. 1990, *ApJ*, **359**, 86
- Edelson, R. A., & Malkan, M. A. 1987, *ApJ*, **323**, 516
- Emmanoulopoulos, D., McHardy, I. M., & Papadakis, I. E. 2013, *MNRAS*, **433**, 907
- Finke, J. 2016, *ApJ*, **830**, 94
- Fuhrmann, L., Larsson, S., Chiang, J., et al. 2014, *MNRAS*, **441**, 1899
- Gaur, H., Mohan, P., Wiercholska, A., & Gu, M. 2018, *MNRAS*, **473**, 3638
- Ghisellini, G., & Tavecchio, F. 2009, *MNRAS*, **397**, 985
- Gu, M., Cao, X., & Jiang, D. R. 2001, *MNRAS*, **327**, 1111
- Gurwell, M. A., Peck, A. B., Hostler, S. R., Darrah, M. R., & Katz, C. A. 2007, in *ASP Conf. Ser.* 375, *From Z-Machines to ALMA: (Sub)Millimeter Spectroscopy of Galaxies*, ed. A. J. Baker et al. (San Francisco, CA: ASP), 234
- Hahn, J. 2015, *Proc. ICRC*, **34**, 917
- Hayashida, M., Madejski, G. M., Nalewajko, K., et al. 2012, *ApJ*, **754**, 114
- Hayashida, M., Nalewajko, K., Madejski, G. M., et al. 2015, *ApJ*, **807**, 79
- Jorstad, S. G., Marscher, A. P., Lister, M. L., et al. 2005, *AJ*, **130**, 1418
- Kalberla, P. M. W., Burton, W. B., Hartmann, D., et al. 2005, *A&A*, **440**, 775
- Larionov, V. M., Villata, M., Raiteri, C. M., et al. 2016, *MNRAS*, **461**, 3047
- Liu, H. T., & Bai, J. M. 2006, *ApJ*, **653**, 1089
- Lynds, C. R., Stockton, A. N., & Livingston, W. C. 1965, *ApJ*, **142**, 1667
- Nilsson, K., Pursimo, T., Villforth, C., Lindfors, E., & Takalo, L. O. 2009, *A&A*, **505**, 601
- Nolan, P. L., Abdo, A. A., Ackermann, M., et al. 2012, *ApJS*, **199**, 31
- Paliya, V. S. 2015, *ApJL*, **808**, L48
- Paliya, V. S., Dilt, C., Bottcher, M., Stalin, C. S., & Buckley, D. 2016, *ApJ*, **817**, 61
- Paliya, V. S., Dilt, C., Bottcher, M., Stalin, C. S., & Buckley, D. 2015a, *ApJ*, **811**, 143
- Paliya, V. S., Sahayanathan, S., & Stalin, C. S. 2015b, *ApJ*, **803**, 15
- Patino-Alvarez, V. M., Dzib, S. A., Lobanov, A., & Chavushyan, V. 2019, *A&A*, **630**, A56
- Peterson, B. M. 2006, *Lecture Notes in Physics*, Vol. 693, *Physics of Active Galactic Nuclei at all Scales* (Berlin: Springer), 77
- Pian, E., Urry, C. M., Maraschi, L., et al. 1999, *ApJ*, **521**, 112
- Pittori, C., Lucarelli, F., Verrecchia, F., et al. 2018, *ApJ*, **856**, 99
- Prince, R. 2019, *ApJ*, **871**, 101
- Prince, R., Raman, G., et al. 2018, *ApJ*, **866**, 16
- Pushkarev, A. B., Kovalev, Y. Y., & Lister, M. L. 2010, *ApJL*, **722**, L7
- Raiteri, C. M., & Villata, M. 2013, *MNRAS*, **436**, 1530
- Rani, B., Krichbaum, T. P., Lee, S. S., et al. 2017, *MNRAS*, **464**, 418
- Richards, J. L., & Max-Moerbeck, W. 2011, *ApJS*, **194**, 29
- Roming, P. W. A., Kennedy, T. E., Mason, K. O., et al. 2005, *SSRv*, **120**, 95
- Schlaflly, E. F., & Finkbeiner, D. P. 2011, *ApJ*, **737**, 103
- Shah, Z., Jithesh, V., Sahayanathan, S., Misra, R., & Iqbal, N. 2019, *MNRAS*, **484**, 3168
- Sikora, M., Begelman, M. C., & Rees, M. J. 1994, *ApJ*, **421**, 153
- Sikora, M., Stawarz, L., Moderski, R., Nalewajko, K., & Madejski, G. M. 2009, *ApJ*, **704**, 38
- Smith, P. S., Montiel, E., Rightley, S., et al. 2009, arXiv:0912.3621
- Urry, C. M., & Padovani, P. 1995, *PASP*, **107**, 803
- Vaughan, S., Edelson, R., Warwick, R. S., et al. 2003, *MNRAS*, **345**, 1271
- Vittorini, V., Tavani, M., & Cavaliere, A. 2017, *ApJL*, **843**, L23
- Woo, J.-H., & Urry, C. M. 2002, *ApJ*, **579**, 530
- Wu, L., Wu, Q., Yan, D., et al. 2018, *ApJ*, **852**, 45
- Yan, D. H., Zhang, L., & Zhang, S. N. 2015, *MNRAS*, **454**, 1310
- Zhang, H., Chen, X., Boettcher, M., Guo, F., & Li, H. 2015, *ApJ*, **804**, 58
- Zhang, Y. H., Celotti, A., Treves, A., et al. 1999, *ApJ*, **527**, 719